IEICE TRANS. COMMUN., VOL.E107–B, NO.6 JUNE 2024

PAPER

A Novel Remote-Tracking Heart Rate Measurement Method Based on Stepping Motor and mm-Wave FMCW Radar

Yaokun HU [†,††a)], ***Student Member***, **Xuanyu PENG** [†††*], ***and*** **Takeshi TODA** [††††**], ***Members***

SUMMARY The subject must be motionless for conventional radar-based non-contact vital signs measurements. Additionally, the measurement range is limited by the design of the radar module itself. Although the accuracy of measurements has been improving, the prospects for their application could have been faster to develop. This paper proposed a novel radar-based adaptive tracking method for measuring the heart rate of the moving monitored person. The radar module is fixed on a circular plate and driven by stepping motors to rotate it. In order to protect the user's privacy, the method uses radar signal processing to detect the subject's position to control a stepping motor that adjusts the radar's measurement range. The results of the fixed-route experiments revealed that when the subject was moving at a speed of 0.5 m/s, the mean values of RMSE for heart rate measurements were all below 2.85 beat per minute (bpm), and when moving at a speed of 1 m/s, they were all below 4.05 bpm. When subjects walked at random routes and speeds, the RMSE of the measurements were all below 6.85 bpm, with a mean value of 4.35 bpm. The average RR interval time of the reconstructed heartbeat signal was highly correlated with the electrocardiography (ECG) data, with a correlation coefficient of 0.9905. In addition, this study not only evaluated the potential effect of arm swing (more normal walking motion) on heart rate measurement but also demonstrated the ability of the proposed method to measure heart rate in a multiple-people scenario.

key words: *FMCW radar, health care, heart rate, radar signal processing, vital sign detection*

1. Introduction

The number of seniors living alone and in nursing homes is rising because of longevity. It is difficult to detect potential medical problems in the body of a senior person. However, cardiovascular disease is the primary cause of death in Japan, accounting for 25.5% of all deaths [1]. The development of an indoor heart rate monitoring system for older people living alone is urgently needed because of this growing social issue.

The conventional contact measures are inappropriate for continuous, round-the-clock monitoring and seniors with skin issues. The research on non-contact radar-based heart rate measurements has recently gained popularity. In [2], they estimated the subject's vital signs were estimated using a millimeter-wave FMCW radar. The authors of [3] proposed a differential enhancement approach and employed an FMCW radar with an 8.4 GHz center carrier frequency to precisely measure the heart rate. In [4], a learning-refined integral null space pursuit algorithm was suggested for adaptively acquiring vital signs with an impulse radio UWB (IR-UWB) radar and a stepped-frequency continuous-wave UWB radar. For non-contact vital sign monitoring, a continuous wave (CW) Doppler radar that operates as a phase-locked loop in a phase-demodulator configuration was proposed in [5].

IR-UWB radar [4], [8], [9], CW Doppler radar [5], [10]–[14], and FMCW radar [2], [15]–[18] are the types of radars that are currently most frequently utilized in this study field. The maximum signal energy levels that can be transmitted are not very high, which reduces the precision and signal-to-noise ratio (SNR) of IR-UWB radars [19]. Likewise, because CW Doppler radar lacks a range capacity [20], measurements are subject to interference and are therefore inappropriate for keeping track of the vital signs of moving targets. The FMCW radar combines the advantages of the first two, with good range and speed measurement capabilities, and the millimeter-band FMCW radar is extremely sensitive. It can effectively measure the displacement of the human skin surface. Therefore, this study employs the FMCW radar in the 77–81 GHz band.

Most radar-based vital signs estimation studies call for subjects to stay still, including standing, sitting in a chair, or resting in bed [2]–[20]. This limits the application of radar-based heart rate measurement methods. For this reason, the authors of [21], [22] and [23] attempted to use IR-UWB radar and FMCW radar, respectively, to estimate the heart rate of a moving person. However, the subjects in the research mentioned above could only move slowly. To address this issue, we proposed an improved adaptive range bin selection (IARBS) method for moving subjects' heart rate measurements based on the FMCW radar [24]. The subjects maintained a high measurement accuracy when they walked at an average speed of 1 m/s. However, because of the radar characteristics, the measurement range may be constrained. It is challenging to cover the entire room, even with beamforming techniques. When the angle is too large, the beam widens, the antenna gain drops, and the perfor-

Manuscript received August 23, 2023.
Manuscript revised October 25, 2023.
Manuscript publicized January 30, 2024.

[†]The author is with the Graduate School of Science and Technology, Nihon University, Tokyo, 101-0062 Japan.
[††]The author is with Fujitsu Ltd., Kawasaki-shi, 211-8588 Japan.
[†††]The author was with the College of Intelligent Manufacturing, Hunan Vocational Institute of Technology, Hunan, 411104 China.
[††††]The author was with Fujitsu Laboratories Ltd., Kawasaki-shi, 211-8588 Japan.
[*]Presently, with the Graduate School of Science and Technology, Nihon University.
[**]Presently, with the College of Science and Technology of Nihon University.
a) E-mail: csgy19014@g.nihon-u.ac.jp
DOI: 10.23919/transcom.2023EBP3143

mance suffers. If there are several radars in the room, they can interfere with each other and increase background noise. Moreover, these methods increase the cost of the measurement system, which is not conducive to the popularity of the application.

The authors of [34] proposed a novel approach for mounting radar on a mobile robot. However, it may not be appropriate for older adults living alone, in senior homes, or in medically isolated observations. There is a safety risk because the senior may trip over the wires because the robot must be attached to the power source. It is difficult to continuously monitor if a charging method is employed. In [26], a method for adaptively changing radar orientation by acquiring the subject's position through a camera was proposed. However, image processing using cameras is sensitive to ambient lighting and involves personal privacy issues. Additionally, the subjects' heart rate measurements while moving were not evaluated in the abovementioned study.

In [27], we proposed and discussed the possibility of using a stepping motor to change the radar orientation but only verified it using a simple simulation. This paper improves the method of [27] and proposes a novel, radar-based, adaptive remote-tracking heart rate measuring technique to address the abovementioned issues. In this study, we build an actual measurement device. The radar module is fixed to a rotatable circular plate. The radar measures the heart rate while measuring the position of the monitored person, which is then processed and transmitted to a stepping motor to drive the rotation of the radar module. A stepping motor is used in this study because for the following reasons. Because the stepping motor has no brushes, it is more reliable. Additionally, it does not accumulate the error of one step to the next step, and thus has better position accuracy. Furthermore, the motor is simple and inexpensive, because its response is based only on a digital input pulse.

The monitored person can always be within the ideal measurement range owing to the adaptively adjusted radar orientation. Next, after sampling the raw radar data, the range bins where the subject is located are selected along the time dimension using the IARBS method, and their phase information is extracted. The displacement information of the human skin surface, brought on by the body's torso, heartbeat, and breathing, can be obtained using the phase change information. We suggested using the improved complete ensemble empirical mode decomposition with adaptive noise (ICEEMDAN) approach to extract the heartbeat signal and determine its heart rate [28]. In this study, we continue to use this technique to analyze the experimental data and evaluate the accuracy of the proposed measurement system.

In this study, we build an actual measurement device, using a stepping motor to change the radar direction to adjust the ideal range for measuring the heart rate. The proposed measurement system tracks a moving subject using radar signal processing. Even though this subject walks at an average speed of 1 m/s and the horizontal angle to the radar module varies widely. This significantly increases the application potential of radar-based remote heart rate measurements. To the best of our knowledge, this is the first study that challenges this field.

The principle of employing FMCW radar to detect vital signs is explained in Sect. 2. The proposed method is explained in detail in Sect. 3. The experiments and conclusions are presented in Sects. 4 and 5, respectively.

2. Principle for Heart Rate Measurements

Figure 1 depicts the structure of the FMCW radar-based heart rate measuring system for moving people. As shown in Fig. 2, the ramp generator periodically outputs an up-chirp signal with a time duration of T_c and frequencies ranging from f_{min} to f_{max} at specific time intervals. The slope of the upward linear frequency modulation of each chirp is K_s, and the sweeping bandwidth is $B = f_{max} - f_{min=}T_cK_s$.

The power amplifier amplifies each chirp signal before transmission. The radar module receives the signal after it is reflected by the object and amplifies it using a low-noise amplifier. The transmitted and the received signals are correlated by the in-phase and quadrature (I/Q) mixer to generate the intermediate frequency (IF) signal. Since there are four receivers (with the same configuration), there are also four IF signals. After the analog-to-digital converter (ADC) samples each IF signal, phase information can be preserved. The sampled raw data are transmitted frame-by-frame to the computer for signal processing. Each IF signal can be defined by the following equation:

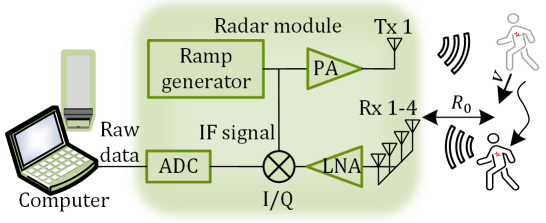

Fig. 1 The block diagram of the FMCW radar module. The analog-to-digital converter, low-noise amplifier, and power amplifier are each denoted by the acronyms PA, LNA, and ADC. The computer receives the raw data to process the signals.

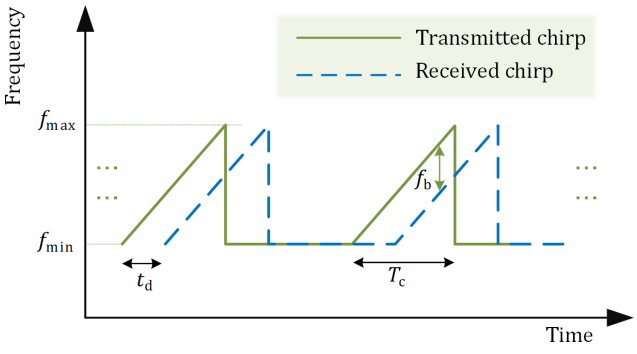

Fig. 2 The time-frequency diagram of the transmitted and received chirps of the case of single Tx and single Rx.

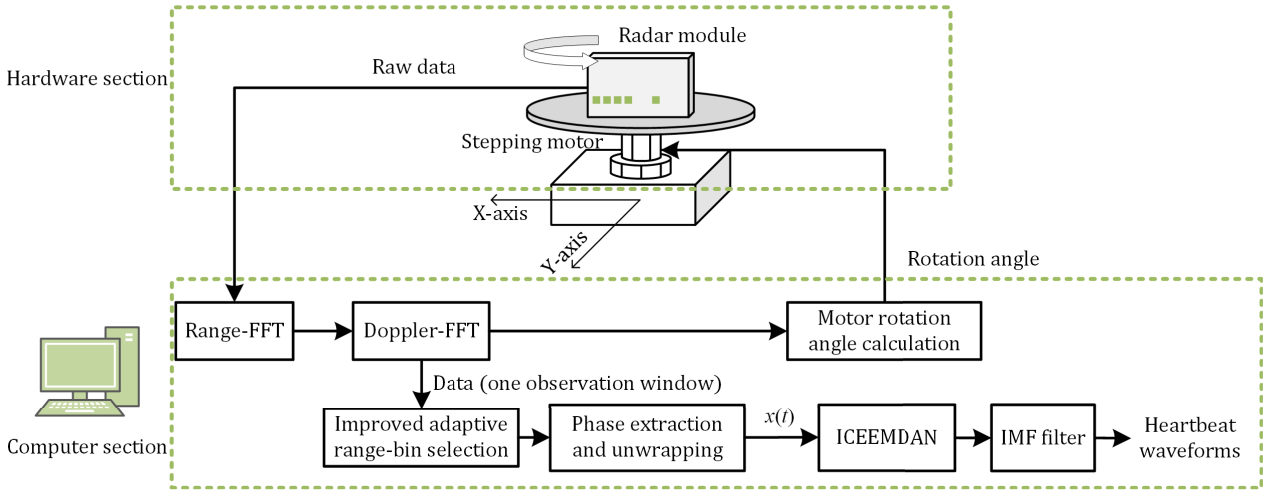

Fig. 3 The flow chart of the proposed processing.

$$s_{\mathrm{if}}(t) = A_{\mathrm{t}}A_{\mathrm{r}} \exp\left(j\left(2\pi f_{\min} t_{\mathrm{d}} + 2\pi K_{\mathrm{s}} t_{\mathrm{d}} t - \pi K_{\mathrm{s}} t_{\mathrm{d}}^2\right)\right)$$
$$\approx A_{\mathrm{t}}A_{\mathrm{r}} \exp\left(j\left(2\pi f_{\min} t_{\mathrm{d}} + 2\pi K_{\mathrm{s}} t_{\mathrm{d}} t\right)\right) t_{\mathrm{d}} < t < T_{\mathrm{c}} \quad (1)$$

where A_{t} is magnitude associated with the transmission power and A_{r} is related to A_{t} by the radar equation. Time delay, t_{d} between the signal being transmitted and received. Because $\pi K_{\mathrm{s}} t_{\mathrm{d}}^2$ in (1) is small, it can be disregarded [2], [28]. The relationship between the instantaneous distance R_0 and delay time t_{d} of the measured target and radar module can be expressed as:

$$R_0 = \frac{\mathrm{c}t_{\mathrm{d}}}{2} \quad (2)$$

where c represents the speed of light. Combining (1) and (2), the frequency of the IF signal and its phase information can be expressed as

$$f_{\mathrm{b}} = \frac{2K_{\mathrm{s}}R_0}{\mathrm{c}}, \quad \varphi(t) = 4\pi f_{\min}\frac{(R_0 + x(t))}{\mathrm{c}} \quad (3)$$

where $x(t)$ can be interpreted as the displacement of the thoracic cavity caused by the heartbeat and breathing of the target. The heart rate estimation can usually be accomplished with only one IF signal.

3. Proposed Measurement System

As mentioned in the introduction, the inability to alter the radar module's orientation is a drawback of conventional radar-based heart rate measurement methods. Therefore, it is impossible to estimate the heart rate once the subject has departed from a specific range. A heart rate measurement method with a motor combined with a millimeter-wave FMCW radar is proposed in this study as a solution to the abovementioned issue and to increase the applicability of the measurement method. The proposed approach utilizes radar signal processing to calculate the target's motion information, which is then sent to a stepping motor to adjust the orientation of the radar module. In this manner, real-time adaptive tracking heart rate monitoring is accomplished.

The signal processing flowchart of the proposed method is shown in Fig. 3, where the computer section is divided into sections for heart rate monitoring and stepping motor rotation control.

3.1 Stepping Motor Rotation Control

The ADC samples the IF signal, which is then sent to a computer in frames for signal processing. In radar-based heart rate measurement research, 0.05 s is a typical choice for the frame period [2], [15]. A frame period T_{f} of 0.05 s is comparable to sampling the target's heartbeat signal at a sampling frequency of 20 Hz because the average human heart rate is less than 2 Hz, which satisfies the sampling theorem. However, excessive shortening of the frame period leads to more frequent data transmission from the radar module to the computer, which may increase the possibility of data loss. Therefore, in this study, the frame length was fixed at 0.05 s.

As shown in Fig. 4, this study emits L chirp signals in a single frame cycle to execute multidimensional FFT calculations, in contrast to other studies that emit only one chirp signal in each frame. A raw data matrix with L rows and N columns is generated for each frame after each chirp signal is sampled N times. A range-FFT is first performed to the fast time dimension of each frame's raw data to generate the range profile matrix (RPM). Next, a Doppler-FFT is applied to the slow time dimension of the RPM to create a range-Doppler matrix (RDM).

A flowchart of the calculation of the rotation angle of the stepping motor is shown in Fig. 5. Assuming a frame period of 0.05 s, the maximum distance moved in a single frame is only 10 cm, even if the subject walks at a higher speed of 2 m/s. Therefore, the distance moved by the subject in a single frame cycle is relatively small, and considering the high real-time requirements of this measurement method, it is not necessary to rotate the motor frame by

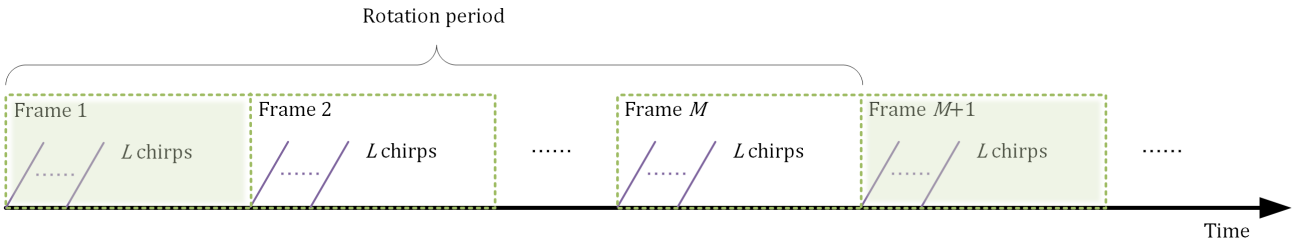

Fig. 4 Diagram of frame period in relation to rotation period.

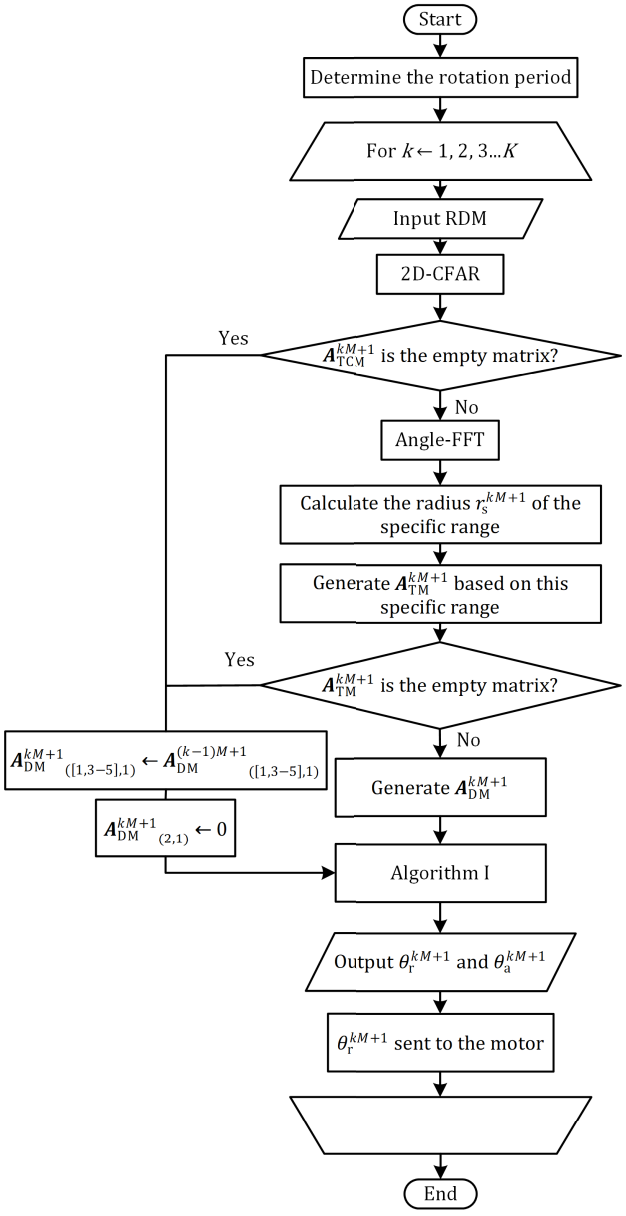

Fig. 5 Flowchart of calculating the rotation angle.

frame. Instead, it determines whether a stepping motor is required to correct the radar alignment by detecting the subject's position every M frames (one rotation period T_r). The motor rotation angle calculation module receives the RDM of the $kM + 1$ th frame ($k = 1, 2, 3, \ldots, K$) as input, as depicted in Fig. 4.

The clutter brought on by other objects and the noise produced by the radar receiver due to temperature, weather, and other factors influence the quality of the radar signal. Therefore, the range bin cells containing the target candidates and their Doppler shifts are identified by performing 2D-CA-CFAR processing for each RDM. 2D-CA-CFAR, 2D-OS-CFAR, and other CFAR algorithms are increasingly being utilized [29], [30]. 2D-OS-CFAR performs better in scenarios with numerous strong interference targets, but the computational effort is substantial [31]. 2D-CA-CFAR is computationally simple and exhibits good performance in pure-noise situations. The 2D-CA-CFAR algorithm is chosen because the environmental background of this study is not complex, the subject is only one person, and the requirement for real-time performance is high. In addition, because the millimeter wave has a high sweep bandwidth, the range bin cell corresponds to a tiny distance interval; therefore, the protection and reference cells of the CA-CFAR algorithm do not affect the measurable range of the radar. CFAR-related algorithms are not the main topic of this work, and the correlations between false alarm probability, judgment threshold, and detection probability are discussed in more detail in [31].

Objects in the RDM that exceed the threshold after 2D-CA-CFAR processing are referred to as target candidates. The instantaneous velocities of the target candidates in the $kM + 1$ th frame are calculated using the Doppler shift. All target candidates, including the subject, remain immobile when the velocities are zero. As a result, the rotation angle θ_r^{kM+1} is zero, and the motor does not need to be adjusted to change the orientation of the radar module.

A target candidate matrix (TCM) $\boldsymbol{A}_{\mathrm{TCM}}^{kM+1}$ is created if u ($u = 1, 2, 3, \ldots, U$) moving targets are detected in the $kM + 1$th frame, with the number of columns representing the number of candidates. The first row is the distance R_{kM+1} from the radar, and the second row represents the instantaneous velocity information v_{kM+1}, as shown in (4).

$$\boldsymbol{A}_{\mathrm{TCM}}^{kM+1} = \begin{bmatrix} R_1^{kM+1} & R_2^{kM+1} & R_3^{kM+1} & \cdots & R_U^{kM+1} \\ v_1^{kM+1} & v_2^{kM+1} & v_3^{kM+1} & \cdots & v_U^{kM+1} \end{bmatrix} \tag{4}$$

The instantaneous angle of the object can be calculated by the following

$$\theta = \sin^{-1} \frac{\lambda \Delta\omega}{2\pi \mathrm{d}}, \tag{5}$$

where λ is the wavelength, $\Delta\omega$ is the phase difference obtained after angle-FFT processing in the antenna direction based on the data obtained by RDM, and d is the pitch of the receiver antennas. The geometric significance of θ is the angle of arrival (AoA) of the object with the radar module in the horizontal plane.

It is assumed that the radar coordinate point is the origin of the coordinate system, and the initial orientation of the radar module is the positive direction of the y-axis, from which the absolute coordinate system is established. The initial position and velocity of the target are $(0, R_1^0)$ and zero, respectively. Additionally, angle $\theta_{\mathrm{a}}^{kM+1}$ is formed by the initial and current radar orientations and is updated in real time. The orientation of the radar changes when tracking the target. Therefore, utilizing $\theta_{\mathrm{a}}^{kM+1}$ to map the target's current coordinates into the initial absolute coordinates is necessary. In this way, the TCM can be expanded to five rows, as shown in (6), with the third row representing the angle information and the fourth and fifth rows representing the x-axis and y-axis absolute coordinates, respectively. The x-axis and y-axis directions are defined in Fig. 3.

$$\boldsymbol{A}_{\mathrm{TCM}}^{0} = \begin{bmatrix} R_1^0 \\ 0 \\ 0 \\ 0 \\ R_1^0 \end{bmatrix},$$

$$\boldsymbol{A}_{\mathrm{TCM}}^{kM+1} = \begin{bmatrix} R_1^{kM+1} & \cdots & R_U^{kM+1} \\ v_1^{kM+1} & \cdots & v_U^{kM+1} \\ \theta_1^{kM+1} & \cdots & \theta_U^{kM+1} \\ R_1^{kM+1}\sin(\theta_1^{kM+1}+\theta_{\mathrm{a}}^{(k-1)M+1}) & \cdots & R_U^{kM+1}\sin(\theta_U^{kM+1}+\theta_{\mathrm{a}}^{(k-1)M+1}) \\ R_1^{kM+1}\cos(\theta_1^{kM+1}+\theta_{\mathrm{a}}^{(k-1)M+1}) & \cdots & R_U^{kM+1}\cos(\theta_U^{kM+1}+\theta_{\mathrm{a}}^{(k-1)M+1}) \end{bmatrix} \tag{6}$$

Although the subject may generate multiple target candidates, clutter may also exist in the TCM. Therefore, a range of values is specified based on the prior motion information of the target, which is very similar to the improved range bin selection method we proposed previously [24]. The distinction is that the specified range of values in this study is expanded from a one-dimensional line to a two-dimensional surface. All target candidates within a specific range are regarded as being produced by the subject and creating a new target matrix $\boldsymbol{A}_{\mathrm{TM}}^{kM+1}$. Then, averaging along each row of the $\boldsymbol{A}_{\mathrm{TM}}^{kM+1}$ yields a rotation decision matrix $\boldsymbol{A}_{\mathrm{DM}}^{kM+1}$ for that frame with one column and five rows, as shown in (7).

$$\boldsymbol{A}_{\mathrm{DM}}^{kM+1} = \begin{bmatrix} \overline{R}^{kM+1} \\ \overline{v}^{kM+1} \\ \overline{\theta}^{kM+1} \\ \overline{R}^{kM+1}\sin\left(\overline{\theta}^{kM+1}+\theta_{\mathrm{a}}^{(k-1)M+1}\right) \\ \overline{R}^{kM+1}\cos\left(\overline{\theta}^{kM+1}+\theta_{\mathrm{a}}^{(k-1)M+1}\right) \end{bmatrix}, \tag{7}$$

where $\overline{\theta}^{kM+1}$ is the angle between the subject and the positive direction of the radar module. To obtain the $\boldsymbol{A}_{\mathrm{TM}}^{kM+1}$, the specific range of values for the current TCM is defined as

1) The center coordinates of the circle are set to the values $\boldsymbol{A}_{\mathrm{DM}\ (4,1)}^{(k-1)M+1}$ and $\boldsymbol{A}_{\mathrm{DM}\ (5,1)}^{(k-1)M+1}$ of the preceding rotation period.

2) The human walking process can be approximated as a uniform motion, so the radius r_{s}^{kM+1} of the specific range of values can be calculated using (8) and (9). The protection unit β_{s} is also introduced to increase fault tolerance, considering that there is occasionally acceleration from the stationary state to the uniform state.

$$r_{\mathrm{s}}^{kM+1} = \left(\left|\overline{v}^{(k-1)M+1}\right| T_{\mathrm{r}}\right) + \beta_{\mathrm{s}}, \tag{8}$$

$$\beta_{\mathrm{s}} = \frac{1}{2} a_{\mathrm{s}} {T_{\mathrm{r}}}^2, \tag{9}$$

where a_{s} is the subject's acceleration, and the value can be adjusted based on the conditions of the environment and the application background.

3) Assume that matrix TCM has u ($u = 1, 2, 3, \ldots, U$) target candidates. Then, the target candidates satisfying (10) are retained to form $\boldsymbol{A}_{\mathrm{TM}}^{kM+1}$. This is compared to the matrix $\boldsymbol{A}_{\mathrm{TCM}}^{0}$ when k is zero.

$$r_{\mathrm{s}}^{kM+1} \geq \sqrt{\left(\boldsymbol{A}_{\mathrm{TCM}\ (4,u)}^{kM+1} - \boldsymbol{A}_{\mathrm{DM}\ (4,1)}^{(k-1)M+1}\right)^2 + \left(\boldsymbol{A}_{\mathrm{TCM}\ (5,u)}^{kM+1} - \boldsymbol{A}_{\mathrm{DM}\ (5,1)}^{(k-1)M+1}\right)^2} \tag{10}$$

When $\boldsymbol{A}_{\mathrm{TCM}}^{kM+1}$ or $\boldsymbol{A}_{\mathrm{TM}}^{kM+1}$ is empty, $\boldsymbol{A}_{\mathrm{DM}}^{kM+1}$ inherits the matrix $\boldsymbol{A}_{\mathrm{DM}}^{(k-1)M+1}$ except for the second element (instantaneous velocity information), because there is no moving target in a particular range. Hence, the value of the second element is zero.

By contrast, $\boldsymbol{A}_{\mathrm{TM}}^{kM+1}$ is averaged along the row direction to produce $\boldsymbol{A}_{\mathrm{DM}}^{kM+1}$ if it is not empty. $\boldsymbol{A}_{\mathrm{DM}\ (3,1)}^{kM+1}$ is the arrival angle of the subject, and its angle with the positive direction of the y-axis in absolute coordinates is $\boldsymbol{A}_{\mathrm{DM}\ (3,1)}^{kM+1} + \theta_{\mathrm{a}}^{(k-1)M+1}$.

The rotation angle threshold value θ_{s} is set to filter angle $\boldsymbol{A}_{\mathrm{DM}\ (3,1)}^{kM+1}$. If the subject's movement results in only a slight angle shift, it is not essential to rotate the motor to change the radar's orientation. Thus, the proposed method can be used to ensure that the subject is always within the measured range and not precisely on the midline of the radar azimuth. Frequent, brief back-and-forth rotations may reduce the accuracy of heart rate measurements. The Algorithm I calculates the angle $\theta_{\mathrm{r}}^{kM+1}$ the motor needs to rotate at each period and updates the angle $\theta_{\mathrm{a}}^{kM+1}$. Finally, the stepping motor operates according to angle $\theta_{\mathrm{r}}^{kM+1}$.

In the multi-subject scenario, regardless of whether the other subjects are stationary, their information will not be included in the $\boldsymbol{A}_{\mathrm{TM}}$ since they are not within a specific range. Usually, the specific range is very small. For example, if the rotation period is 0.2 s and the average speed is 1 m/s, the

Algorithm I Rotation Angle Calculation

θ_{step} is the step angle of the stepping motor (a constant parameter);

$\lceil \ldots \rceil$ rounds the element to the next larger integer ;

$\lfloor \ldots \rfloor$ rounds the element down to the next lower integer ;

If $A_{\text{DM}}^{kM+1}{}_{(3,1)} < \theta_{\text{s}}$ **then**

$\theta_{\text{r}}^{kM+1} \leftarrow 0$;

$\theta_{\text{a}}^{kM+1} \leftarrow \theta_{\text{a}}^{(k-1)M+1}$;

Else

If $A_{\text{DM}}^{kM+1}{}_{(3,1)} > 0$ **then**

$$\theta_{\text{r}}^{kM+1} \leftarrow \left\lceil \frac{A_{\text{DM}}^{kM+1}{}_{(3,1)}}{\theta_{\text{step}}} \right\rceil \theta_{\text{step}} ;$$

Else

$$\theta_{\text{r}}^{kM+1} \leftarrow \left\lfloor \frac{A_{\text{DM}}^{kM+1}{}_{(3,1)}}{\theta_{\text{step}}} \right\rfloor \theta_{\text{step}} ;$$

$\theta_{\text{a}}^{kM+1} \leftarrow \theta_{\text{a}}^{(k-1)M+1} + \theta_{\text{r}}^{kM+1}$;

Return: $\theta_{\text{r}}^{kM+1}, \theta_{\text{a}}^{kM+1}$;

radius of the search range is only about 0.2 m. The probability of other subjects entering this range is very low. An object may generate more than one target candidate point. Even if the other subjects are close to the tracked subject, only a few points from other subjects exist within the specific range. Then, the average processing in the calculation of $\boldsymbol{A}_{\text{DM}}$ will remove their effect. Therefore, the proposed tracking method can also correctly lock the target without interference from other subjects in a multi-subject scenario.

3.2 Heart Rate Monitoring

The approach mentioned above ensures that the subject is constantly within the measurement range. By examining the RPM, the phase change information $\varphi(t)$ can be obtained from the range bin cell where the subject is located. The thoracic skin displacement $x(t)$ is determined by using the phase change information, and this displacement is then utilized to extract the heartbeat signal and determine the heart rate.

As discussed in the introduction, subjects had to remain still (sitting, standing, or lying down) for the measurement in most earlier studies using radar-based heart rate monitoring. In addition, the subjects were typically close to the radar. In this situation, techniques such as RPM peak detection can quickly identify the range bin cell in which the subject is located. Furthermore, once the range bin cell is located, no further modifications are required for the duration of the measuring cycle.

In contrast, the subjects in this study were accompanied by two states, motion and stationary, implying that the target range bin cells were constantly changing. Additionally, because RPM peak-seeking or RDM peak-seeking is susceptible to noise, it is challenging to locate the target range bin cells using these methods alone. Therefore, we suggested the improved adaptive range bin selection approach [24], which is also utilized in this study, to collect high-quality phase information precisely and swiftly.

The initial location confirmation and adaptive range bin selection are two parts of the IARBS method. The initial DRM $\boldsymbol{D}_{\text{i}}$ is obtained in the first step by immediately accumulating the up-chirp signals of H frames, which ensures that the appropriate range bin cell $\alpha_{\text{optimal}}^{H}$ is acquired at the beginning.

In the second stage, starting with frame $H+1$, the instantaneous velocity of the subject, as determined by the data from the preceding frames, adaptively limits the peak-seeking range of the DRM for each frame. The following are the justifications for not directly using the data from matrix $\boldsymbol{A}_{\text{DM}}$. High real-time performance is needed for motor rotation, and the rotation angle calculation function quickly calculates the subject's approximate position per M frames. However, heart rate measurement must precisely obtain the optimal range bin cell.

$\alpha_{\text{max}}^{H+j}$, $\alpha_{\text{min}}^{H+j}$, and $\alpha_{\text{optimal}}^{H+j}$ are the upper and lower bounds of the peak-seeking range and the outcomes for frame $H+j$ ($j = 1, 2, 3, \ldots, J$), respectively. Their relationship is defined by (11), (12), and (13).

$$\alpha_{\text{min}}^{H+j} = \alpha_{\text{optimal}}^{H+(j-1)} - \left\lceil \frac{v_{\text{m}}^{H+j} T_{\text{f}}}{R_{\text{bin}}} \right\rceil - \beta_{\text{p}}^{H+j}, \tag{11}$$

$$\alpha_{\text{max}}^{H+j} = \alpha_{\text{optimal}}^{H+(j-1)} + \left\lceil \frac{v_{\text{m}}^{H+j} T_{\text{f}}}{R_{\text{bin}}} \right\rceil + \beta_{\text{p}}^{H+j}, \tag{12}$$

$$\beta_{\text{p}}^{H+j} = \left\lceil \eta \left(\frac{\alpha_{\text{max}}^{H+j} - \alpha_{\text{min}}^{H+j} + 1}{2} \right) \right\rceil, \tag{13}$$

where $\lceil \ldots \rceil$ rounds the element to the next larger integer, and R_{bin} represents the length of each range bin cell. The instantaneous velocity of the subject from frame $H+(j-1)$ to frame $H+j$ is represented by v_{m}^{H+j}. The coefficient η ($0 \leq \eta \leq 1$) and the peak-seeking range determine the protection cell length, represented as β_{p}^{H+j}. H and η are typically set at 0.5 and 0.1, respectively, according to [24].

After choosing the optimal range bin cell, L phase information (L chirp signals per frame) can be collected for each frame and averaged to enhance the phase quality. This implies that each frame extracts a phase value in the optimal range bin to which it corresponds. Then, the phase information of each frame in an observation window is stitched together in order of time, which gives the phase information $\varphi(t)$ over time.

Sudden body shaking or noise may occur during the measurement, and longer observation windows will provide better immunity to interference. The measurement will also be more accurate because the longer the data, the higher is the resolution of the FFT bins. In contrast, a shorter observation window provides a better real-time performance. The length of the observation window should be adjusted according to the application. In addition, if the subsequent windows are consecutive, the first stage of the IARBS method can be skipped after processing for the first observation window. Finally, the subject's thoracic displacement $x(t)$ is determined using (3).

Along with the heartbeat signal, $x(t)$ includes the respiration signal and other noises (e.g., body and radar shaking). Wavelet transform and bandpass filter are two techniques for

extracting heartbeat signals [32]–[35]. However, these conventional techniques have limitations because the heartbeat signal differs from person to person and the human heart rate is close to the high-order harmonics of the respiratory frequency.

An improved empirical mode decomposition (EMD) method called ICEEMDAN can adaptively divide a signal into a limited number of intrinsic mode functions (IMFs) depending on the time scale of the signal [36], [37]. Therefore, this study uses the ICEEMDAN method to decompose the $x(t)$ and reconstruct the heartbeat signal, which was confirmed in our previous work. The relationship between $x(t)$ and each IMF, and the residual $r_n(t)$ is given by (14).

$$x(t) = \sum_{i=1}^{n} IMF_i(t) + r_n(t) \quad i = 1, 2, 3, \ldots, n \tag{14}$$

Then all IMFs perform a spectral analysis. The IMF with energy concentrated at 0.8 Hz to 2.0 Hz as heart IMF is extracted to reconstruct the heartbeat signal, and the heart rate can be calculated [28].

4. Experiment

4.1 Equipment

In this experiment, a stepping motor with the specification NEMA17 was employed, and an Arduino UNO development board was used to connect the motor to the computer. The angle information of the subject was transmitted from the computer to the Arduino via serial communication. This motor is a hybrid stepping motor that combines the benefits of reactive and permanent magnet types. It has a high resolution, speed, and torque, and the specific parameters are listed in Table 1.

The radar module used in this research was based on Texas Instruments Inc. IWR1443. It operates at frequencies in the 77–81 GHz range and can continuously chirp up to 4 GHz. However, the radar module can only send chirp signals with a bandwidth of 3.6 GHz during operation, owing to local laws in Japan. Furthermore, the maximum effective isotropic radiated power (EIRP) complies with the Japanese Radio Law and the FFC regulations. It does not cause harm to the human body. In contrast to the SISO mode used by traditional heart rate measurement techniques, in this study, the radar uses a 1Tx4Rx mode to gather data on the subject's angle. The main parameters of the radar module are listed in Table 2.

Although the MIMO mode provides a better angular resolution than the SIMO mode, the SIMO mode is utilized in this study for the following reasons.

First, the background of this application is the medical monitoring of older people living alone. In most cases, there is typically no interference from other moving targets after screening using range-FFT and Doppler-FFT processing.

Second, as discussed in Sect. 3, after locking the target subject using the proposed method, the range of the current target selection is restricted to the spatial plane based on the target position of the previous rotation period. Therefore, even if other subjects are present during the measurement procedure, the proposed method ensures that there is no interference from them.

Third, employing the 3Tx4Rx mode for radar will inevitably increase the frame period and the amount of computation. This will reduce the real-time performance of the motor rotation and lead to the possibility that the subject will be out of the measurement range. The SISO data is utilized to calculate the chest displacement; hence, switching to the MIMO mode while maintaining a constant frame time will reduce the length of the SISO data. The phase quality of the IF signal is subsequently reduced. To increase measurement accuracy, this study focus on the phase quality of the IF signal rather than just the angular precision and angular resolution of the target subject.

In addition, we proposed in [24] a measurement method to simultaneously measure the heart rate of multiple people while walking. The proposed method for this study tracks a target subject and measures the vital signs, aiming to maximize the measurement range. Theoretically, it can also obtain the vital signs of other people within the measurement range. Moreover, the motor rotation angle calculation algorithm can be initialized to change the target subject.

A physical diagram of the hardware is shown in Fig. 6. A bracket holds the radar module on a circular plate, and the stepping motor rotates the plate. A DC power supply feeds the motor.

Table 1 Motor parameters list.

Type	Bipolar stepping motor
Stepping angle	1.8 deg.
Stepping mode	Full-step
Hold torque	5500 g·cm
Rated voltage	12 V
Rated current	1.5 A

Table 2 Radar module main parameters.

Parameter	Value
Bandwidth	3.6 GHz
Sweep time	51.4 µs
Frame length	50 ms
Slope	70 MHz/µs

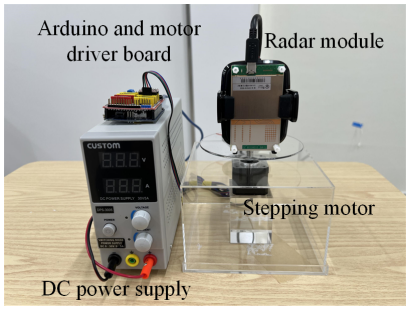

Fig. 6 The physical diagram of the hardware.

4.2 Experimental Environment and Route

The experiment for this study has four parts: a fixed route experiment, a random route experiment, an arm swing (more normal walking motion) comparison experiment, and a multi-subject scenario experiment.

There are five fixed routes, A, B, C, D, and E, as shown in Fig. 7(a) and (b). Routes A, B, and C are horizontal lines with midpoints of 0.5, 1, and 1.5 m from the radar module, and their ends are at an angle of 90 degrees from the radar. Move along a straight line with an average speed of roughly 0.5 m/s and 1 m/s, starting at the right endpoint of each route. For simplicity, the routes are denoted as A1, B1, C1 (average speed of 0.5 m/s), and A2, B2, and C2 (average speed of 1 m/s), respectively. The x-axis and y-axis directions are also defined in the various subplots of Fig. 7.

Route D is a 180-degree arc with a radius of one meter centered on the radar coordinates. The starting point coordinates are $(1, 0)$ and also move with an average speed of 0.5 m/s (route D1) and 1 m/s (route D2), respectively.

The above routes evaluate the feasibility of the proposed method, whereas route E is considered for its applicability. The subject traveled down route E in a 4 m × 2 m rectangle at a typical walking speed of 1 m/s. Furthermore, in the fixed route experiment, the subject attempted to face the radar module with either the front or back of the body.

The random route is then a free walk within a 4.5 × 5 square meter area in front of the radar module to further measure the practical application potential of the proposed method.

There are two routes for the arm swing comparison experiment, as shown in Fig. 7(d). Routes F1 and G1 indicate scenes without arm swings, whereas F2 and G2 indicate scenes with arm swings. The subjects moved along the route back and forth at an average speed of no more than 1 m/s.

The multi-subject scenario experiment aims to demonstrate that the proposed measurement system can precisely track the target subject in this case. This experiment was conducted with three subjects simultaneously, as shown in Fig. 7(e). Subject I, as the target, walked back and forth between 0.5 m and 3.5 m in front of the radar at an average speed of no more than 1 m/s (with the arm swing). Subjects II and III walked randomly along a horizontal straight line 1 and 3 m from the front of the radar, respectively. This experiment can observe whether the orientation of the radar is interfered with by other people while the measurement system tracks subject I.

The subjects alternated between walking and constantly standing during each measurement period of 60 s to simulate the movement of people in the room. Figure 8 depicts the actual experimental scenario. Additionally, the subject wore an ECG device to record heart rate data during the measurement.

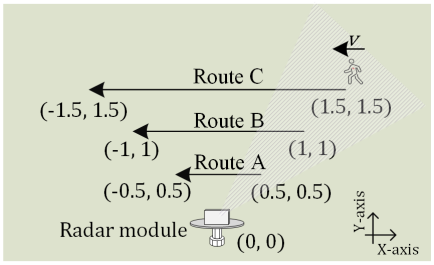

(a)

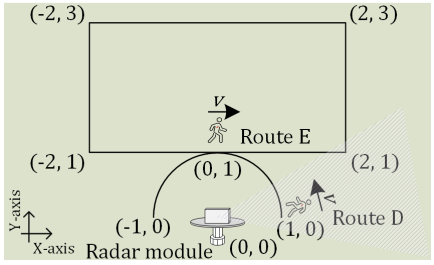

(b)

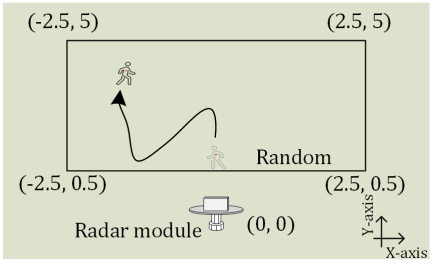

(c)

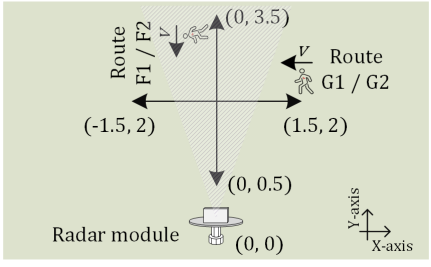

(d)

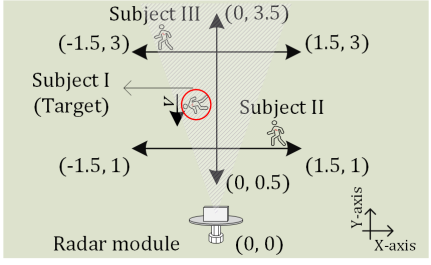

(e)

Fig. 7 Walking route maps of subjects.

(a) Non-swinging arm scenario

(b) Arm swing scenario

(c) Multi-subject scenario

Fig. 8 Experiment scenarios.

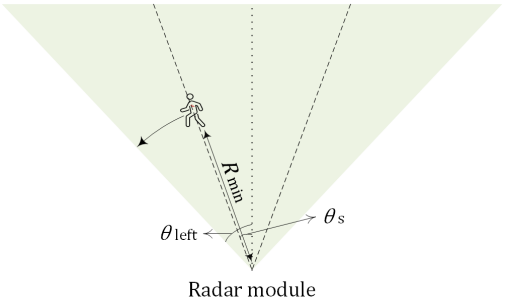

Fig. 9 The figure depicts how to select the appropriate minimum rotation angle by the half-power angle of radar.

4.3 Parameter Analysis

The radar's horizontal left-half power angle is θ_{left}, and the minimum measurement distance is $R_{\min}$. The following equation must be satisfied by the variables M and θ_s.

$$MT_f v_p < \frac{|\theta_{\text{left}} - \theta_s|\,\pi R_{\min}}{180^\circ}, \tag{15}$$

where v_p is the speed at which the person moves under normal conditions. As shown in Fig. 9, assume that the subject's distance from the radar is precisely $R_{\min}$ and that the subject's angle with the radar centerline is infinitesimally close to θ_s. In the next rotation period, the possible walking distance of the subject is at most $MT_f v_p$ to ensure that it is within the measurement range. In the context of the application of this measurement system, elderly individuals who live alone typically do not move indoors at speeds greater than 1 m/s. This experiment sets M and θ_s to 4 and 5 degrees because $R_{\min}$ is 0.5 m and the half-power angle of azimuth and elevation are about 70 and 10 degrees, respectively.

Table 3 Information about subjects.

Subject	Height [cm]	Weight [kg]
A	175	60
B	170	56
C	169	60
D	174	61
E	176	62
F	166	78

4.4 Experimental Results

Six volunteers participated in this experiment, and Table 3 lists their heights and weights. In order to better evaluate the proposed approach, it is necessary to reduce the variable factors between the different subjects as much as possible. Therefore, the height of the radar module was adjusted according to the thoracic height of the volunteer before the beginning of the measurement to try to keep both at the same horizontal plane. Each volunteer participated in all the routes of this experiment.

Figure 10 shows the cumulative distribution functions (CDF) of the absolute values of the measured AoA ($|\text{Angle}|$: $\left|\boldsymbol{A}_{\text{DM}}^{kM+1}{}_{(3,1)}\right|$) for each rotation period of the fixed route and the random route experiments for all subjects. Overall, the subjects remained within the ideal measurement range of plus or minus 35 degrees in front of the radar throughout the measurement cycle.

Owing to the subjects' faster angular velocity, as they moved along route A, the AoA values for route A were greater than those measured for the other routes. The results for routes B and C showed that in 90 percent of cases, the subjects had an AoA of less than 10 degrees. The AoA values increased with the movement speed of the subject. However, the effect is not particularly substantial, according to the combined results of all fixed route experiments.

The results for route D show that the measurement system tracks accurately even when the subject's angle changes by up to 180 degrees. Accordingly, depending on the requirements of the application, it is possible to position the radar module in the center of the room for 360-degree tracking measures. The angular velocity of the subject relative to the radar during route D was higher than that of routes A, B, and C, which led to a more significant difference in the results of the CDF of routes D1 and D2 than the other routes. In addition, the measurement system can accurately track the subject during random walks. In a few cases, the angle of the subject's position was approximately 30 degrees. However, no subject's position was outside the ideal measurement range, which demonstrates the reliability of the system.

Because route E contains straight lines similar to routes A-C, Fig. 11 shows only the results of the traced trail for one

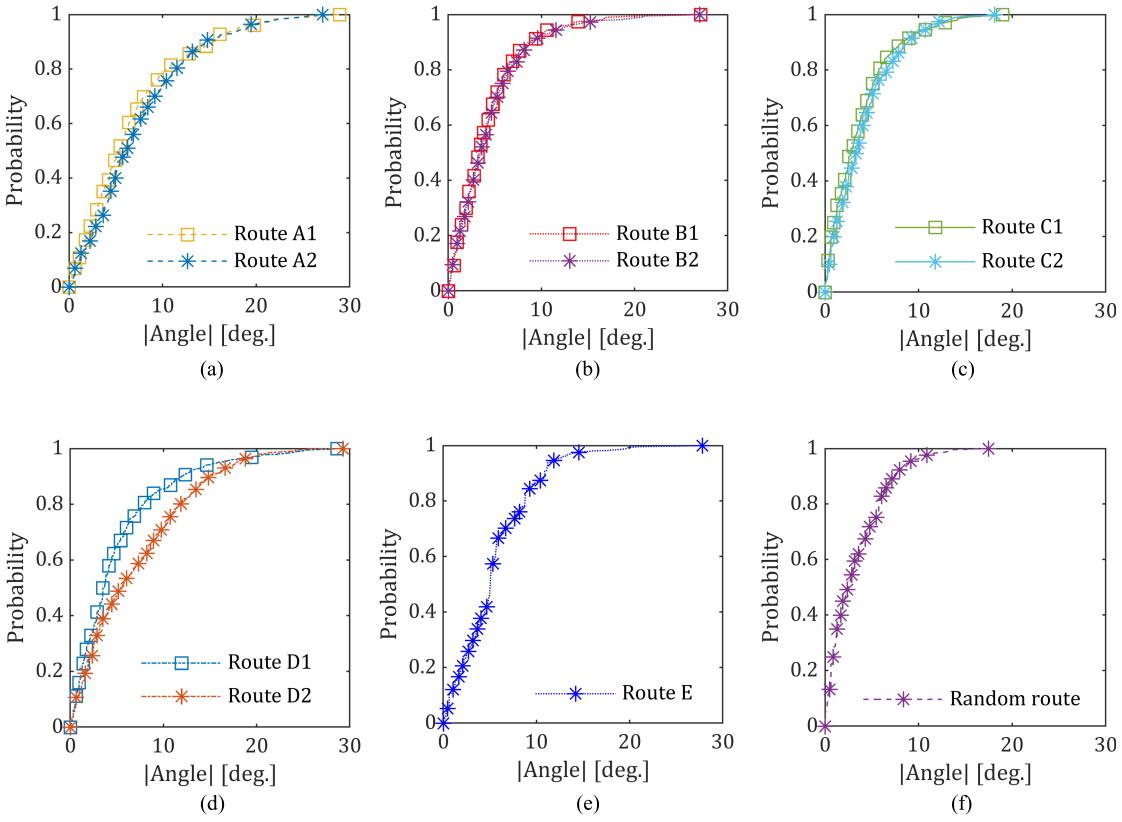

Fig. 10 The cumulative distribution functions of the absolute values of the measured subject's angle information.

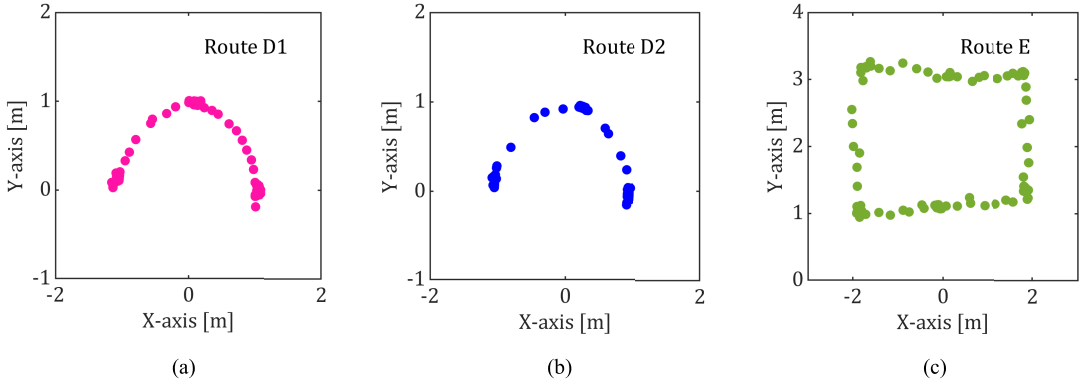

Fig. 11 The results of the traced trail for one subject walking along routes D and E.

subject walking along routes D and E. The results show that the tracking trail is still rather precise, even if the proposed method quickly detects the subject's approximate location and sends it to the motor.

The RPM of a subject walking along route D2 and the optimal range bin results achieved by the IARBS method are shown in Fig. 12(a) and (b). The phases extracted from the optimal range bins are then stitched together along the slow time dimension to calculate the $x(t)$ of the subject, as shown in Fig. 12(c).

Next, $x(t)$ was decomposed into a finite number of IMFs using the ICEEMDAN method. FFT processing is performed on them to select the heart IMF among IMFs. The analysis was performed with a 30 s observation window. The results after decomposition by ICEEMDAN are shown in Fig. 13, with the time and frequency domains of each IMF on the left and right, respectively. According to the frequency domain analysis, the heart IMF and breathing IMF were IMF_3 and IMF_5. This study focused on the heartbeat signal because the breathing signal is a low-frequency component that is simple to extract. Finally, the heartbeat signal was reconstructed. Finally, IMF_3 was used to reconstruct the heartbeat signal and estimate the heart rate.

In addition, the phase change data and low-frequency

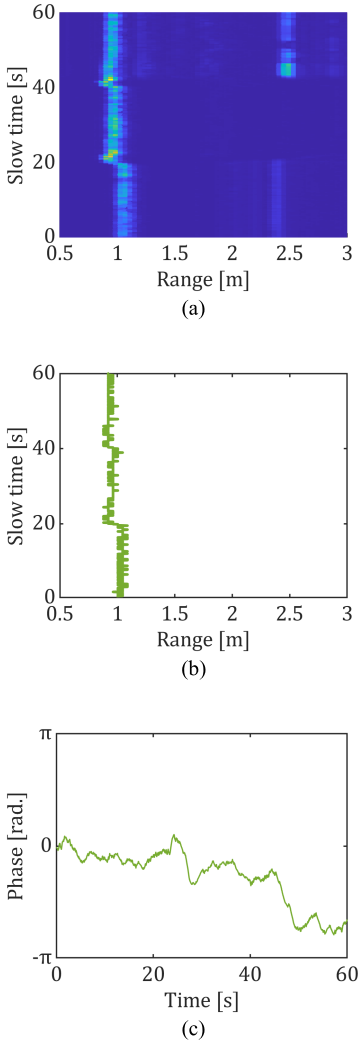

Fig. 12 The RPM (a) of a subject walking along route D2, the optimal range bin results (b) achieved by the IARBS method, and the stitched phase change information (c) are shown in this figure.

IMFs demonstrate that walking causes the $x(t)$ signal to vary more than when the subject is motionless [28].

Figure 14(a) shows a frequency domain comparison of the reconstructed heartbeat signal and ECG signal. These measurement data were obtained using route D2. The heart rates obtained by the proposed method and ECG were 1.767 Hz and 1.833 Hz, respectively, with an absolute error of approximately 3.96 beats per minute (bpm), and the accuracy was approximately 96.4%.

The spectrum of the measurements is wider than that of the ECG. The following are some of the possible reasons for this phenomenon. Firstly, there is a fundamental difference between ECG, an electrical signal, and radar-based heart rate measurement, measured by a displacement signal from the skin. Secondly, the human chest skin is not plane, and the skin displacement caused by the heartbeat is slightly different at each location. Thirdly, the subject was walking, and there was inevitably a small amount of noise compared to stationary. The ICEEMDAN method has minimized the

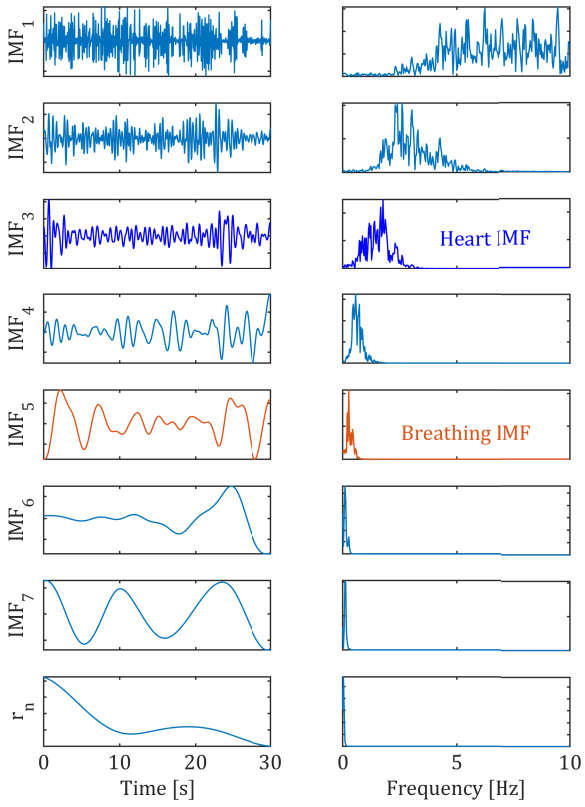

Fig. 13 Results of ICEEMDAN decomposition. The left and right sides are the time domain and frequency domain, respectively.

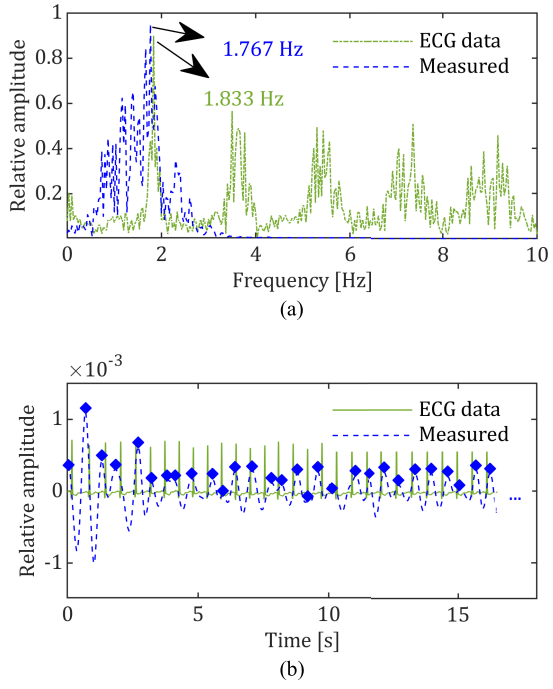

Fig. 14 (a) The frequency domain comparison of the reconstructed heartbeat signal and the ECG signal. (b) The time domain comparison of the reconstructed heartbeat waveforms and the ECG waveform.

Table 4 Accuracy of heart rate measurement [%].

Route	A1	A2	B1	B2	E
Mean	98.42	97.47	97.29	96.78	97.19
Route	C1	C2	D1	D2	Random
Mean	97.69	96.64	98.06	97.08	96.16
Route	F1	F2	G1	G2	Multi-subject
Mean	97.05	96.75	97.83	97.27	96.22

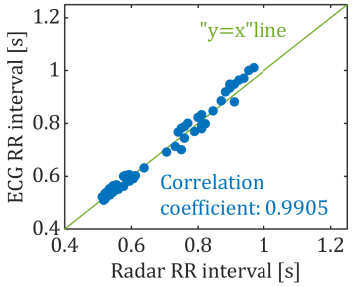

Fig. 15 The correlation of the RR interval measured by radar with ECG data.

amplitude of the interference term as much as possible. In this research field, the most attention is paid to the accuracy of heart rate and RR interval measurements. Therefore, the practicality of the proposed method is not affected.

Table 4 lists the average heart rate measurement accuracy for each route. The accuracy increased with proximity to the radar or slower speeds, and route A1 had the highest measurement accuracy at 98.42%. The results of routes F and G show that swinging the arm while walking decreases the accuracy of the heart rate measurement by approximately 0.3% to 0.56%. The accuracy of the heart rate measurements decreased by 0.53%, while other people interfered. The overall average measurement accuracy, including the random route, was above 96%, thus maintaining a high level of accuracy.

To better observe the details, a portion of the reconstructed heartbeat waveform is compared with its corresponding ECG waveform in the time domain, as shown in Fig. 14(b). The results showed a higher correlation between the measured heartbeat waveform's RR interval (spacing between rhombuses) and the ECG data. Meanwhile, Fig. 15 depicts the correlation between the mean RR interval time of all measurements of the fixed route experiment, random route experiment, and the corresponding ECG. The radar and ECG data were the horizontal and vertical coordinates, respectively. The correlation coefficient γ of the two datasets was calculated using (16), and their correlation coefficient was 0.9905, indicating a high correlation between them.

$$\gamma = \frac{1}{P-1}\sum_{i=1}^{P}\left(\frac{F_i-\mu F}{\sigma F}\right)\left(\frac{E_i-\mu E}{\sigma E}\right), \tag{16}$$

where P and i are the total number of data and their indices, respectively. F is the data measured by the radar and E is the ECG data used as a reference. The means of the two data are μF and μE and their standard deviations are σF and σE. Figure 16 shows the CDF of the absolute error of all fixed

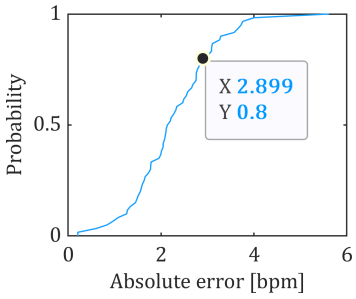

Fig. 16 The cumulative distribution functions of the absolute error of heart rate measurement.

Table 5 The RMSE of heart rate measurement (the fixed and random route experiment) [BPM].

Route \ Subject	A	B	C	D	E	F	Mean
A1	1.99	1.75	1.88	2.05	1.89	1.79	1.89
A2	3.71	3.38	3.78	2.68	3.94	1.86	3.23
B1	2.57	2.55	3.66	3.58	3.52	1.14	2.84
B2	3.99	3.82	4.67	3.85	3.25	3.74	3.89
C1	2.30	2.34	3.67	3.32	2.00	2.75	2.73
C2	5.32	3.03	4.25	3.72	3.86	4.03	4.04
D1	2.46	2.77	3.02	1.78	2.67	2.01	2.45
D2	2.64	3.91	3.83	5.23	3.05	3.44	3.68
E	4.01	2.42	3.73	5.39	2.45	4.00	3.67
Random	6.64	2.31	6.82	6.33	2.58	1.42	4.35

and random route experiment measurements. In 80% of the measurements, the absolute error was under 2.9 bpm. There were no instances when the absolute error exceeded 6 bpm, even when the random route results were considered.

To further quantitatively analyze the proposed method's heart rate measurement results, 60 s streaming data were analyzed with a 30 s observation window and a 1 s sliding step. Then, the heart rate for each observation window is calculated and contrasted with the ECG data to determine the root mean square error (RMSE), as shown in (17).

$$\mathrm{RMSE} = \sqrt{\frac{1}{Q}\sum_{i=1}^{Q}(HRR_i - HRE_i)^2}, \tag{17}$$

where Q and i are the total number of observation windows and their index numbers, respectively. *HRR* and *HRE* are the heart rates measured by each observation window and reference heart rate (ECG data), respectively.

Table 5 presents the RMSE of the heart rate measurements of the fixed and random route experiments. The results demonstrate that as the distance and speed increase, the RMSE of the heart rate estimation also increases. According to the average RMSE value for each route, the RMSE is approximately 1.2 bpm lower when the subject walks at 0.5 m/s as opposed to 1 m/s. We speculate that precision may be affected because the stepping motor rotates more frequently, causing the fixed plate to vibrate and generate noise. Meanwhile, the experimental results of [24] demonstrated that the speed of the subject can affect how accurately the IARBS method chooses the optimal range bin. Additionally, the positive association between RMSE and

Table 6 The RMSE of heart rate measurement (the arm swing comparison experiment) [BPM].

Route \ Subject	A	B	C	D	E	F	Mean
F1 (No arm swinging)	3.46	1.64	2.59	3.13	3.49	3.59	2.98
F2 (Arm swinging)	3.67	3.45	2.50	3.19	3.85	4.18	3.47
G1 (No arm swinging)	3.44	3.26	4.02	3.41	3.95	4.00	3.68
G2 (Arm swinging)	4.37	3.32	4.75	2.77	4.06	4.32	3.93

distance will rise less quickly or stop being significant if the subject's distance from the radar exceeds 1 m. Likewise, when the subject moves at a speed of 1 m/s, the rate at which the RMSE increases with distance will decrease. Therefore, the experimental results showed that the RMSE values of the proposed method for heart rate estimation converged to a particular value and were stable.

The heart rate estimates are highly accurate even when the subject's angle information changes significantly, as evidenced by the mean RMSEs of 2.45 bpm and 3.68 bpm for routes D1 and D2, respectively. The results for each volunteer in the random route experiment varied significantly. However, the RMSEs were all below 6.9 bpm, with a mean value of 4.35 bpm. Some of the larger RMSEs are caused by spending extended periods with the side of the body facing the radar, which decreases the measurement accuracy.

Table 6 presents the RMSE of the arm swing comparison experiment's heart rate measurements. Notwithstanding individual variations, swinging of the subject's arm throughout the measurement process can affect the measurement accuracy. During the arm swing, the average RMSE of routes F and G decreased by 0.49 bpm and 0.25 bpm, respectively. This influence is caused by the left anterior thoracic muscle movement when the arm is swung, and the movement of the upper arm also causes a change in the phase of the IF signal.

Figure 17(a), (b), and (c) depict the RPM of the multi-subject scenario experiment, the RDM of a certain frame during the measurement, and the optimal range bin results of the target subject achieved by the IARBS method, respectively. The target subject was within the measurement range at all times and the rotation of the radar module was not disturbed by other people. Figure 17(b) shows the RDM when the target subject and other subjects overlapped on the RPM. The IARBS method can adaptively adjust the peak-seeking range based on the velocity of the target subject in the previous time. It is robust to other subjects suddenly entering its peak-seeking range. Even if other subjects are at the same range bin as the target subject for an extended time, their heart rates can be separated by the ICEEMDAN method. Figure 17(c) shows that the IARBS method can accurately select the optimal range bin of the target subject in the multi-subject scenario. However, there are many interference factors in this case, such as the possible presence of multiple subjects' arm swings and body shaking simultaneously in one range bin cell.

As discussed in Sect. 3, longer observation windows result in better interference immunity. Figure 18 compares the heart IMF and ECG data in the frequency domain for each observation window in the multi-subject scenario experiment. The ECG data showed that the mean heart rate during the measurement period was 1.402 Hz. No significant peaks in the heart IMF made it challenging to estimate the heart rate, whether the observation window was 30, 40, or 50 s. The peak frequency is 1.417 Hz when the observation window is 60 s, and the absolute error is about 0.9 bpm compared to the ECG data, with an accuracy of 98.93%. The measurement accuracies of the six subjects were 95.37%, 98.93%, 95.55%, 96.28%, 95.49%, and 95.69%, respectively, with a mean value of 96.22%. The measurement accuracy of this experiment was also influenced by the random movements of the non-target subjects, which were similar to the random route experiment. The experimental results show that the heart rate measurement for the target subject

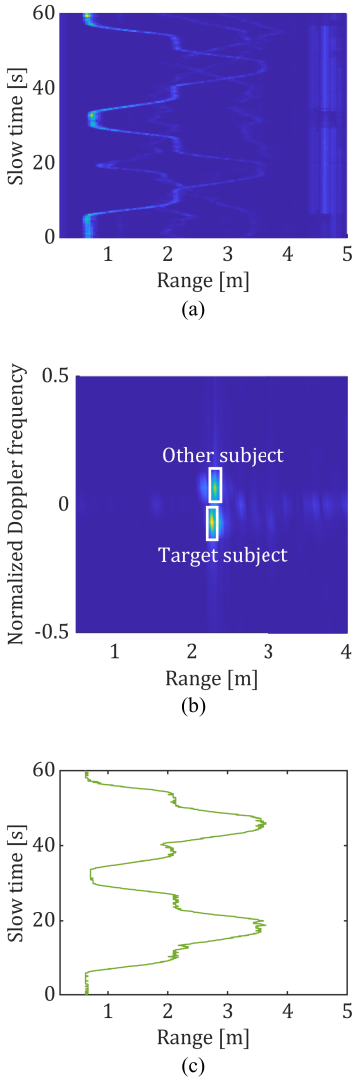

Fig. 17 The RPM (a) of the multi-subject scenario experiment, the RDM (b) of a certain frame during the measurement, and the optimal range bin results (c) of the target subject achieved by the IARBS method are shown in this figure.

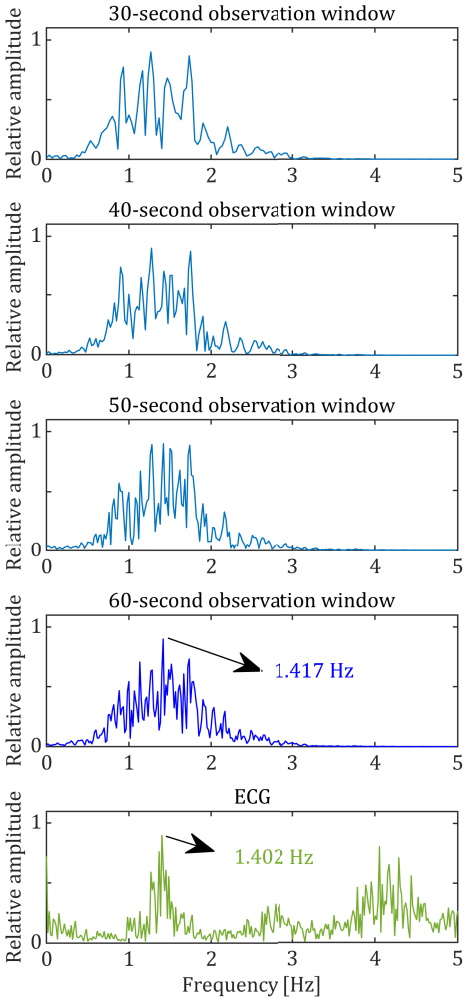

Fig. 18 Comparison of heart IMF and ECG data in the frequency domain for each observation window in the multi-subject scenario experiment.

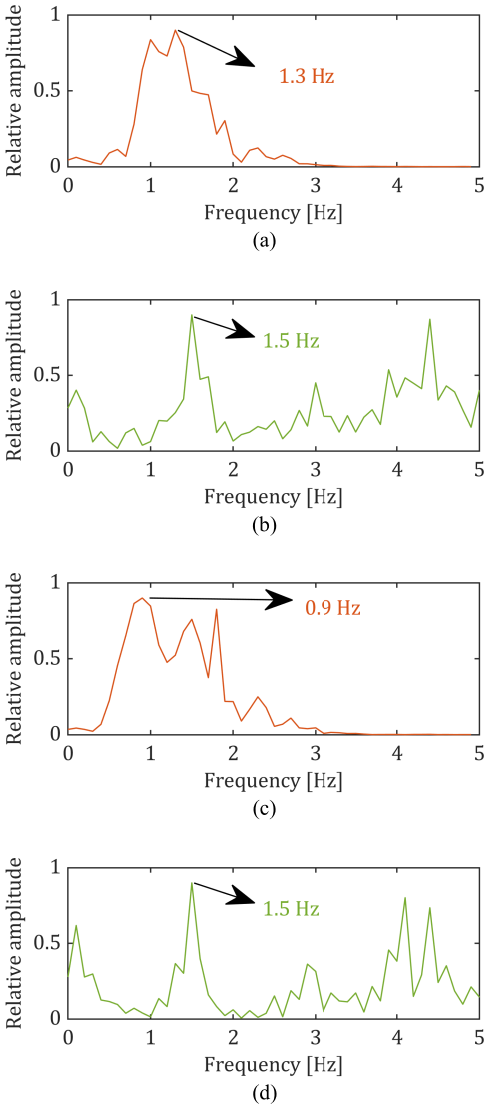

Fig. 19 In (a) and (c), the two spectrums of heart IMF were measured with a 10-second observation window, and the ECG data corresponding to them are shown in (b) and (d).

still maintains a high accuracy in multiple people scenarios.

In addition, it is challenging to improve real-time performance by shortening the observation window whenever heart rate is measured using FFT-based time-frequency domain analysis, including the ICEEMDAN method. For example, when the frame period is 0.05 s (typical), and the observation window is below 10 s and 5 s, the spectrum's frequency resolution will be as low as 0.1 Hz and 0.2 Hz. Meanwhile, the EMD-based algorithm (ICEEMDAN) is required for the data's length, which is not sufficient to separate the individual frequency components if it is too short. [15], [28] using EMD-based algorithms to measure heart rate with the subject at stationary have employed an observation window of at least 15 s. Since the subject in this study was moving, the evaluation was attempted with an observation window of 30 s or more.

Figure 19 shows two spectrums of heart IMF measured with a 10-second observation window. As shown in Fig. 19(a) and (b), the heart rate can be easily detected when interference is low in the spectrum of the heart IMF. However, the low frequency resolution of the spectrum resulted in a measurement error of 0.2 Hz. Due to the shortness of the data, heart rate estimation will become difficult when ICEEMDAN cannot efficiently extract high-quality, low-interference heart IMF, as shown in Fig. 19(c) and (d). Interference occurs randomly, and clearly, longer observation windows possess better robustness.

In order to trade off the real-time performance and stability of the measurement system, the following attempts are considered in future work. One is to shorten the frame period as much as possible to increase the data length, provided the radar hardware supports it. The other one is that the application uses an overall delayed dynamic display when displaying heartbeat waveforms. The next measurement and processing are performed simultaneously during the previous waveform display. When the previous waveform is just about finished, the next waveform is displayed immediately afterward.

Because this study is the first to estimate the heart rate by adjusting the radar measurement range through stepping motors, the measurement results are difficult to compare quantitatively with other papers. Therefore, the main focus is the qualitative comparison and analysis of this experiment's results with those of other works' measurements.

Most radar-based heart rate estimation methods, such as those in [2]–[20], cannot perform tracking measurements on moving targets, whereas the proposed method offers this possibility.

In the experiment in [23], the subject moved slowly and the heart rate was measured with 90% accuracy. In [21], the subjects made only backward and forward movements with a measurement error range of 0–8 bpm. By contrast, the subjects in this experiment were faster, and the RMSEs of the measurements were all below 7 bpm. Moreover, the average measurement accuracy for each route exceeded 96%. The measurement accuracy in our previous study [24] was 95.88%. This is because the subject was consistently inside the ideal measurement range in this experiment, which increased the accuracy.

The six participants in [15] were in a stationary state. At distances of 1 m, 1.5 m, 2 m, and 2.5 m from the radar, the mean values of the RMSE for heart rate estimation were approximately 2.39 bpm, 2.57 bpm, 3.23 bpm, and 4.69 bpm, respectively. Although the results for routes B and C were higher than 2.39 and 2.57 bpm, the farthest distance in route E was about 3.61 m, and the mean value of RMSE was only 3.67 bpm. In addition, the proposed method can change the radar orientation to adjust the measurement range and estimate the heart rate of a moving person, making it more advantageous for application.

5. Conclusion

In conclusion, this study proposes a novel radar-based adaptive tracking method for measuring the heart rate of a moving subject. The proposed algorithm is employed to determine the position of the subject to control a stepping motor that adjusts the radar measurement range. The results of the fixed-route experiments revealed that when the subject was moving at a speed of 0.5 m/s, the mean values of RMSE for heart rate measurements were all below 2.85 bpm, and when moving at a speed of 1 m/s, they were all below 4.05 bpm. When subjects walked at random routes and speeds, the RMSE of the measurements were all below 6.85 bpm, with a mean value of 4.35 bpm. In addition, this study not only evaluated the potential effect of arm swing (more normal walking motion) on heart rate measurement but also demonstrated the ability of the proposed method to measure heart rate in a multiple-person scenario.

Meanwhile, the overall measurement accuracy was greater than 96%, when the random route was included. Moreover, the RR intervals of the reconstructed heartbeat signal and ECG data were highly correlated, with a correlation coefficient of 0.9905. In the future, we plan to improve the experimental platform to reduce the noise generated by the radar as it rotates to improve the accuracy of the measurements.

Acknowledgments

This study was supported by the School of Science and Technology, College of Science and Technology, Nihon University. This study involved human subjects in its research. Approval of all ethical and experimental procedures and protocols was granted by the Nihon University Research Ethics Guideline. The authors would like to thank Kosuke Otsu for his help in collecting the experimental data.

References

[1] S. Yasuda, Y. Miyamoto, and H. Ogawa, "Current status of cardiovascular medicine in the aging society of Japan," Circulation, vol.138, no.10, pp.965–967, Sept. 2018.
[2] M. Alizadeh, G. Shaker, J.C.M.D. Almeida, P.P. Morita, and S. Safavi-Naeini, "Remote monitoring of human vital signs using mm-wave FMCW radar," IEEE Access, vol.7, pp.54958–54968, 2019.
[3] Y. Xiong, Z. Peng, C. Gu, S. Li, D. Wang, and W. Zhang, "Differential enhancement method for robust and accurate heart rate monitoring via microwave vital sign sensing," IEEE Trans. Instrum. Meas., vol.69, no.9, pp.7108–7118, Sept. 2020.
[4] L. Qiao X. Li, B. Xiao, M. He, X. Bi, W. Li, and X. Gao, "Learning-refined integral null space pursuit algorithm for noncontact multi-subjects vital signs measurements using SFCW-UWB and IR-UWB radar," IEEE Trans. Instrum. Meas., vol.71, pp.1–13, 2022.
[5] M. Mercuri, Y. Liu, I. Lorato, T. Torfs, F. Wieringa, A. Bourdoux, and C.V. Hoof, "A direct phase-tracking Doppler radar using wavelet independent component analysis for non-contact respiratory and heart rate monitoring," IEEE Trans. Biomed. Circuits Syst., vol.12, no.3, pp.632–643, June 2018.
[6] D. Yang, Z. Zhu, and B. Liang, "Vital sign signal extraction method based on permutation entropy and EEMD algorithm for ultra-wideband radar," IEEE Access, vol.7, pp.178879–178890, Dec. 2019
[7] X. Shang, J. Liu, and J. Li, "Multiple object localization and vital sign monitoring using IR-UWB MIMO radar," IEEE Trans. Aerosp. Electron. Syst., vol.56, no.6, pp.4437–4450, Dec. 2020.
[8] H. Shen, C. Xu, Y. Yang, L. Sun, Z. Cai, L. Bai, E. Clancy, and X. Huang, "Respiration and heartbeat rates measurement based on autocorrelation using IR-UWB radar," IEEE Trans. Circuits Syst. II, Exp. Briefs, vol.65, no.10, pp.1470–1474, Oct. 2018.
[9] P. Wang, F. Qi, M. Liu, F. Liang, H. Xue, Y. Zhang, H. Lv, and J. Wang "Noncontact heart rate measurement based on an improved convolutional sparse coding method using IR-UWB radar," IEEE Access, vol.7, pp.158492–158502, Oct. 2019.
[10] W. Xia, Y. Li, and S. Dong, "Radar-based high-accuracy cardiac activity sensing," IEEE Trans. Instrum. Meas., vol.70, pp.1–13, 2021.
[11] V.L. Petrović, M.M. Janković, A.V. Lupšić, V.R. Mihajlović and J.S. Popović-Božović, "High-accuracy real-time monitoring of heart rate variability using 24 GHz continuous-wave Doppler radar," IEEE Access, vol.7, pp.74721–74733, 2019.
[12] J. Park, Y. Jeong, G. Lee, J. Oh, and J. Yang, "915-MHz continuous-wave Doppler radar sensor for detection of vital signs," Electronics, vol.8, no.5, 561, 2019.
[13] M. Mercuri, Y. Liu, I. Lorato, T. Torfs, F. Wieringa, A. Bourdoux, and C.V. Hoof, "A direct phase-tracking Doppler radar using wavelet independent component analysis for non-contact respiratory and heart rate monitoring," IEEE Trans. Biomed. Circuits Syst., vol.12, no.3, pp.632–643, June 2018.
[14] N.T. Phuong Nguyen, P.-Y. Lyu, M.H. Lin, C.-C. Chang, and S.-F.

Chang, "A short-time autocorrelation method for noncontact detection of heart rate variability using CW Doppler radar," 2019 IEEE MTT-S International Microwave Biomedical Conference (IMBioC), pp.1–4, 2019.
[15] L. Sun, S. Huang, Y. Li, C. Gu, H. Pan, H. Hong, and X. Zhu, "Remote measurement of human vital signs based on joint-range adaptive EEMD," IEEE Access, vol.8, pp.68514–68524, April 2020.
[16] X. Zhang, Z. Liu, Y. Kong, and C. Li, "Mutual interference suppression using signal separation and adaptive mode decomposition in noncontact vital sign measurements," IEEE Trans. Instrum. Meas., vol.71, no.4001015, pp.1–15, 2022.
[17] T.K.V. Dai, K. Oleksak, T. Kvelashvili, F. Foroughian, C. Bauder, P. Theilmann, A.E. Fathy, and O. Kilic, "Enhancement of remote vital sign monitoring detection accuracy using multiple-input multiple-output 77 GHz FMCW radar," IEEE J. Electromagn. RF Microw. Med. Biol., vol.6, no.1, pp.111–122, March 2022.
[18] J. Liu, Y. Li, C. Li, C. Gu, and J.-F. Mao, "Accurate measurement of human vital signs with linear FMCW radars under proximity stationary clutters," IEEE Trans. Biomed. Circuits Syst., vol.15, no.6, pp.1393–1404, Dec. 2021.
[19] G. Wang, J. Muñoz-Ferreras, C. Gu, C. Li and R. Gómez-García, "Application of linear-frequency-modulated continuous-wave (LFMCW) radars for tracking of vital signs," IEEE Trans. Microw. Theory Techn., vol.62, no.6, pp.1387–1399, June 2014.
[20] G. Wang, C. Gu, T. Inoue, and C. Li, "A hybrid FMCW-interferometry radar for indoor precise positioning and versatile life activity monitoring," IEEE Trans. Microw. Theory Techn., vol.62, no.11, pp.2812–2822, Nov. 2014.
[21] Y. Rong, K.V. Mishra, and D.W. Bliss, "Multiple moving targets heartbeat estimation and recovery using multi-frequency radars," 2021 IEEE Radar Conference (RadarConf21), pp.1–5, 2021.
[22] X. Yang, X. Zhang, H. Qian, Y. Ding, and L. Zhang, "MMT-HEAR: Multiple moving targets heartbeats estimation and recovery using IR-UWB radars," 2020 42nd Annual International Conference of the IEEE Engineering in Medicine & Biology Society (EMBC), pp.5733–5736, 2020.
[23] A. Morimatsu, S. Matsuguma, and A. Kajiwara, "Heart rate estimation of a moving person using 79 GHz-band UWB radar," 2019 IEEE Sensors Applications Symposium (SAS), Sophia Antipolis, France, pp.1–5, May 2019.
[24] Y. Hu and T. Toda, "Remote vital signs measurement of indoor walking persons using mm-wave FMCW radar," IEEE Access, vol.10, pp.78219–78230, July 2022.
[25] P. Zhao, C.X. Lu, B. Wang, C. Chen, L. Xie, M. Wang, N. Trigoni, and A. Markham, "Heart rate sensing with a robot mounted mmWave radar," 2020 IEEE International Conference on Robotics and Automation (ICRA), pp.2812–2818, Aug. 2020.
[26] K. Gupta, Srinivas M.B., Soumya J, O.J. Pandey, and L.R. Cenkeramaddi, "Automatic contact-less monitoring of breathing rate and heart rate utilizing the fusion of mmWave radar and camera steering system," IEEE Sensors J., vol.22, no.22, pp.22179–22191, Nov. 2022.
[27] X. Peng, Y. Hu, and T. Toda, "Design and evaluation of remote tracking heart rate measurement based on millimeter-wave FMCW radar," IEICE Commun. Express, vol.11, no.6, pp.330–335, June 2022.
[28] Y. Hu and T. Toda, "The effect of multi-directional on remote heart rate measurement using PA-LI joint ICEEMDAN method with mm-wave FMCW radar," IEICE Trans. Commun., vol.E105-B, no.2, pp.159–167, Feb. 2022.
[29] Q. Zheng, L. Yang, J. Li, T. Hu, J. Zhu, C. Song, and Z. Xu, "A target detection scheme with decreased complexity and enhanced performance for range-Doppler FMCW radar," IEEE Trans. Instrum. Meas., vol.70, no.8001113, pp.1–13, 2021.
[30] V.V. Tien, T. Vu Hop, L.H. Nam, N. Van Loi, and T.T. Thanh, "An adaptive 2D-OS-CFAR thresholding in clutter environments: Test with real data," 2018 5th International Conference on Signal Processing and Integrated Networks (SPIN), pp.116–119, Sept. 2018.
[31] M. Kronauge and H. Rohling, "Fast two-dimensional CFAR procedure," IEEE Trans. Aerosp. Electron. Syst., vol.49, no.3, pp.1817–1823, July 2013.
[32] D.R. Morgan and M.G. Zierdt, "Novel signal processing techniques for Doppler radar cardiopulmonary sensing," Signal Processing, vol.89, no.1, pp.45–66, Jan. 2009.
[33] T.K.V. Dai, Y. Yu, P. Theilmann, A.E. Fathy, and O. Kilic, "Remote vital sign monitoring with reduced random body swaying motion using heartbeat template and wavelet transform based on constellation diagrams," IEEE J. Electromagn. RF Microw. Med. Biol., vol.6, no.3, pp.429–436, Jan. 2022.
[34] S. Sato, Y. Hu, and T. Toda, "A study of multi-directional heart-rate-estimation with discrete wavelet transform and band pass filter with 77 GHz-band FMCW radar," IEICE 1st Int. Conf. on Emerging Technologies for Communs. (ICETC), G1-4, Dec. 2020.
[35] M. Li and J. Lin, "Wavelet-transform-based data-length-variation technique for fast heart rate detection using 5.8-GHz CW Doppler radar," IEEE Trans. Microw. Theory Techn., vol.66, no.1, pp.568–576, Jan. 2018.
[36] N.E. Huang, Z. Shen, S.R. Long, M.L.C. Wu, H.H. Shih, Q. Zheng, N.C. Yen, C. Tung, and H.H. Liu, "The empirical mode decomposition and the Hilbert spectrum for nonlinear and non-stationary time series analysis," Proc. R. Soc. Lond. A, vol.454, no.1971, pp.903–995, March 1998
[37] M.A. Colominas, G. Schlotthauer, and M.E. Torres, "Improve complete ensemble EMD: A suitable tool for biomedical signal processing," Biomedical Signal Processing and Control, vol.14, pp.19–29, Nov. 2014.

Yaokun Hu received his B.E. degree in electrical engineering and automation from the College of Electric Information, Hunan Institute of Engineering, China, in 2017, and his M.E. degree in electrical engineering from the Graduate School of Science and Technology, Nihon University, Japan, in 2021, respectively. He is currently pursuing a Ph.D. degree in electrical engineering at the Graduate School of Science and Technology, Nihon University, Japan. He joined Fujitsu Ltd., Japan, in 2021, and is working in R&D. His current research interests include radar signal processing, biomedical signal processing, and machine learning.

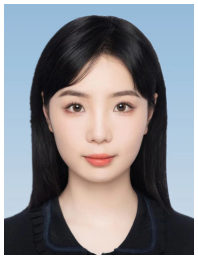

Xuanyu Peng received her B.E. degree in electrical engineering and automation from the College of Electric Information, Hunan Institute of Engineering, China, in 2017, and her M.S. degree in electromechanical engineering from the Faculty of Science and Technology, University of Macau, Macau S.A.R, China, in 2020, respectively. From 2020 to 2023, she was an assistant teacher at the College of Intelligent Manufacturing, Hunan Vocational Institute of Technology, China. From 2023, She will be pursuing a Ph.D. degree in electrical engineering at the Graduate School of Science and Technology, Nihon University, Japan. Her current research interests include signal processing, control algorithms and intelligent robots.

Takeshi Toda received a B.E. degree in electrical engineering from Nihon University, Tokyo, Japan in 1992, an M.S. degree in electronic engineering from the University of Electro-Communications, Tokyo, Japan in 1994, and a D.E. degree from the Tokyo Institute of Technology, Tokyo, Japan in 2004. From 1994 to 2004, he worked at Fujitsu Laboratories Ltd., Kawasaki, Japan. From 2004 to 2005, he worked at eAccess Ltd., in Tokyo, Japan. From 2005 to 2008, he worked at the Kyocera Corp., R&D Center, Yokohama, Japan. He is currently a professor at the College of Science and Technology, Nihon University, Tokyo, Japan. His current research interests include radar signal processing, machine learning, and system-information engineering.